# Comparison of different infiltration amounts of CeO$_2$ inside Ni-YSZ anodes to improve stability and efficiency of Single-Chamber SOFCs operating in methane

*Giovanni* d'Andrea[1,*], *Enrico* Squizzato[1], and *Antonella* Glisenti[1,2]

[1] Department of Chemical Sciences, University of Padova, Via F. Marzolo 1, 35131, Padova, Italy
[2] ICMATE - Department of Chemical Sciences, University of Padova, Via F. Marzolo 1, 35131, Padova, Italy

**Abstract.** Electrochemically active oxide-based anodes capable of working in Single-Chamber Solid Oxide Fuel Cells (SC-SOFCs) were developed. Their performance is related to the selectivity of the electrodes. Tests are carried out on lab-scale devices with YSZ pellets as solid electrolytes in electrolyte supported cells. Selecting methane as a fuel, a gas mixture in the ratio CH$_4$/O$_2$ = 2 was chosen. The Ni-YSZ (NiO:YSZ=60:40) anode was optimized through CeO$_2$ nanocatalysts infiltration to enhance the anode catalytic activity and make its reduction easier. Several infiltration amounts were compared, from null to 15% of the electrode weight. Both symmetric and complete cells (with LSCF-based cathodes) were tested in H$_2$ and CH$_4$/O$_2$. For increasing amounts of infiltrated CeO$_2$, symmetric cells tests describe an area specific resistance (ASR) reduction from 40 $\Omega$ cm$^2$ to 1.7 $\Omega$ cm$^2$ in hydrogen and from 11 $\Omega$ cm$^2$ to 3.9 $\Omega$ cm$^2$ in the methane/oxygen mixture. While complete cells tests displayed an ASR drop from 30 $\Omega$ cm$^2$ to 2.9 $\Omega$ cm$^2$ in H$_2$, and from 8.7 $\Omega$ cm$^2$ to 4.3 $\Omega$ cm$^2$ in the methane/oxygen mixture, while OCP and power grew from 478 mV and 3.7 mW cm$^{-2}$ to 766 mV and 13 mW cm$^{-2}$.

## 1 Introduction

Single Chamber Solid Oxide Fuel Cells (SC-SOFCs) represent a particular branch of SOFCs technologies that aims to overcome the main flows of the dual chamber devices, mainly due to the sealing, that makes the device design more complex and make it hard to be employed for portable applications [1]. Some of the greatest benefits of single chamber SOFCs are the easier fabrication, the great potential for miniaturization, the easier preparation of a stack assembly and the presence of exothermic reactions to sustain the cell temperature [2,3]. Despite the advantages, the main challenges bound to this technology are the intrinsic necessity for highly selective and catalytically active materials, the lower fuel utilization and efficiency, due to parasitic reactions, and the risk of explosion due to fuel and air being mixed together at high temperatures [4,5]. These critical aspects made research on single chambers to become little appealing in the latest years [6], yet its employment for specific applications would make it a competitive technology, as in portable power applications [7], cogeneration [8] or in a context where the high fuel use efficiency is not a fundamental requirement, as sensors [9] or in residual fuel in engine exhaust [10].

Of all possible fuels, methane is a largely available and safe one. In fact, methane must undergo partial oxidation on the anode surface to produce syngas, which is the actual fuel [4,5]. Because of catalytic activity toward the partial oxidation of methane, Ni is the most used catalyst [11,12],

despite it is far from being an ideal catalyst [13,14]. Ni-YSZ is one of the most employed anodic materials, even though YSZ is not an ideal material for intermediate temperature applications, below 700°C [4], however, this ionic conductor has great chemical and mechanical stability. Metal oxides can boost the activity of the anode [15–17]. They are often investigated and represent ideal catalysts whenever balance between costs and performance improvement is reached. Doping with precious metals like Pd or Ru, is not a preferential option though. A material often accounted for in catalysis is CeO$_2$ [18], a promising material for improving Ni-YSZ anode efficiency. Different approaches have been followed to couple these materials, i.e. preparing a solid solution [19] and by infiltration [20]. In this last case, in the work of Yang *et al.* (2014), it was emphasized the stability of the infiltrated CeO$_2$ nano-catalysts, their ability to catalyse the deep oxidation of methane and their ability in helping the reduction of NiO to Ni. The infiltrated amount was 3% of the weight (3wt%) of the NiO-YSZ unreduced electrode.

Aim of this work, was to test the correlation between the anode performance in SC-SOFCs and the increasing infiltration amount of CeO$_2$ into the electrode (3wt%, 6wt%, 9wt% and 15wt%). This was mainly done by means of Electrochemical Impedance Spectroscopy (EIS) where the spectra variation can give insights on a modified ability of the electrode to retain and conduct electrical charge and influence the reaction rate of the fuel. It was chosen to employ a CH$_4$/O$_2$=2 ratio for safety reasons, to work above the upper flammability level [2], and to avoid the redox

---

* Corresponding author: giovanni.dandrea.1@unipd.it

oscillatory behaviour, but it is still high enough to avoid carbon deposition [21]. To maximize the TPB density, it was chosen to employ YSZ as electrolyte, limiting the ability of the material to work on lower temperatures. LSCF was chosen as cathode material. Considering different parameters, like activity towards the oxidation of methane and stability in $CH_4/O_2$ mixtures, seems to be one of the most promising material for SC-SOFCs applications [22]. Due to compatibility issues, a GDC interlayer was employed, paying attention to thermal gradients, for the different thermal expansion coefficient between GDC and YSZ may give rise to complications [23]. The final cathode was LSCF:GDC (50:50) to avoid delamination of pure LSCF cathodes after thermal treatment.

## 2 Experimental

Electrolyte supported cells consisted in YSZ pellets, 1.4 mm thick and 19 mm in diameter, with 12 mm electrodes deposited above via tape casting. YSZ powder was chosen in the stoichiometric ratio of 8YSZ $((Y_2O_3)_{0,08} (ZrO_2)_{0,92})$ (fuelcellmaterials, US). 2.5 g of powder were pressed by a hydraulic press to obtain the pellets that were later oven sintered at 1500°C and eventually polished on P220 sandpaper. Anode powder was produced by impregnation, starting from YSZ powder and $Ni(II)(NO_3)_2 \cdot 6H_2O$ (Sigma-Aldrich, US). To achieve the anode material, with chosen ratio of NiO:YSZ=60:40, the Nickel precursor was mixed with YSZ powder, water and twice its mole amount of citric acid. Keeping the reaction slurry heated and under stirring, basification occurred to obtain pH = 7. After that, the slurry was dried and taken to the ignition point through heating. Eventually, the powder was milled with a mortar and calcinated for 6 hours at 900°C, delivering a pale green powder. To produce the ink, the powder was mixed with 3wt% of carbon soot as a pore former, half its weight in a thinner ink (fuelcellmaterials, US) and a few drops of terpineol based ink vehicle to adjust viscosity (fuelcellmaterials, US). Cathode and interlayer (IL) inks preparation followed the same route, with the cathode consisting in a 50:50 (weight) mixture of LSCF $(La_{0.6}Sr_{0.4}Co_{0.2}Fe_{0.8}O_{3-\delta})$ powder (Sigma-Aldrich, US) and GDC $(Ce_{0.9}Gd_{0.1}O_{1.95})$ powder (fuelcellmaterials, US) and the IL in pure GDC. The electrode inks were deposited above the electrolyte surface with a tape casting technique, where a 12 mm in diameter mask consisted in a punched through piece of packaging tape, and the spreader, in a razor blade. Eventually, the anode was calcinated at 1400°C, while the cathode and the IL, at 1200°C. For complete cells, the cathode was deposited above the GDC interlayer, for which, a 14 mm in diameter mask was used to avoid contact between the cathode and the electrolyte [24]. In fact, as a compatibility test proved, LSCF and YSZ are not compatible materials at 1200°C. In Figure 1, it is reported the XRD pattern of LSCF and YSZ powders mixed together and treated at 1200°C, proving that, even though no insulting phase $La_2Zr_2O_7$ [25], was observed, LSCF structure was completely lost, in favour of simple oxides structures. Cathode calcination at a lower temperature was tested, at 850°C, but no adhesion was achieved, making it impossible to be used in a cell. Even
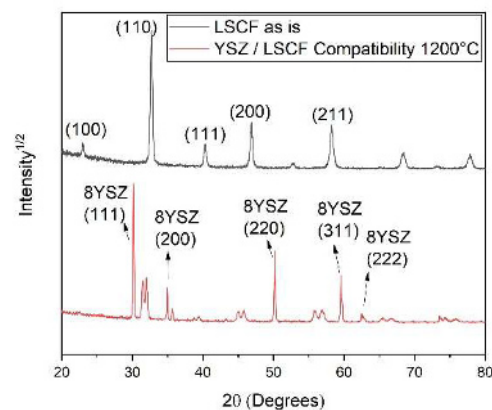


**Figure 1:** Comparison between pure LSCF (black) and the LSCF/YSZ compatibility test at 1200°C powders (red) XRD patterns. LSCF is completely lost after treatment at 1200°C when mixed with YSZ.
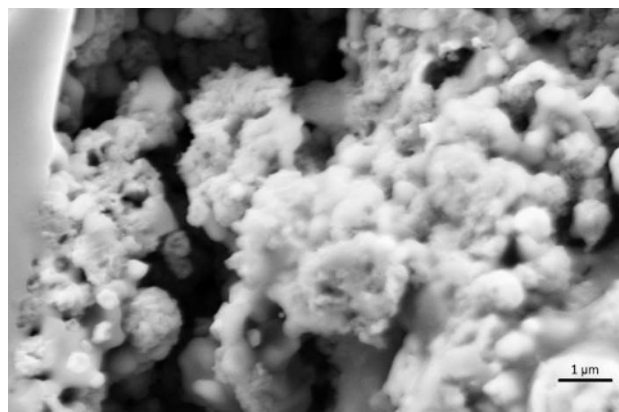


**Figure 2:** SEM image of the NiO-YSZ anode 3wt% $CeO_2$ infiltrated. On the bottom left corner, it is easy to identify the $CeO_2$ nanoparticles.

though, the mixed powders at 850°C did not react together and the two phases remained unchanged. At first an attempt with a $CeO_2$ interlayer was made [26], calcinating the powder at 1200°C, but there was no adhesion on the pellet. The GDC interlayer calcinated at 1200°C have a fair adhesion, but a small portion of powder can be easily removed from the calcinated layer with scotch tape or friction. Since the interlayer, due to its thickness and limited conductivity, decreases the ability of the material to deliver power, it is desirable to keep it as porous and thin as possible, reason why a higher calcination temperature, to give more compactness to the material, was not tested. Also, at higher temperatures it is likely favoured the reaction between Ceria and Zirconia.

Subsequent infiltrations were carried out through weighting the anode, with one measurement of the cell before deposition and after calcination. Infiltration volumes of a 0.5 M $Ce(III)(NO_3)_3$ solution were evaluated on the weight amount of $CeO_2$ expected to be present inside the electrode. After the infiltration of no more than 3wt% at a time, to allow the solution to permeate, the cell was heated to 450°C to let the nitrates decompose and leave $CeO_2$ alone in the structure. In Figure 2, the anode at the interface with the electrolyte is seen and on the bottom
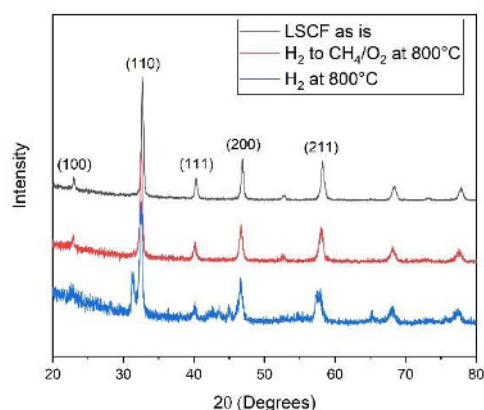
**Figure 3:** Comparison of the XRD patterns for pure LSCF powders (black); the LSCF powders treated at 800°C in $H_2$ first and in $CH_4/O_2$ later (red), preserving the original pattern; and LSCF powders treated at 800°C in $H_2$ (blue), losing the original pattern, showing the formation of new phases.

left corner it is possible to identify the infiltrated $CeO_2$ nanoparticles.

The electrical contacts were obtained using a gold paste (fuelcellmaterials, US) spread on top of the electrodes, then treated at 780°C to decompose the organic carrier, and a gold wire cemented in contact with it.

The first challenge was to identify the best reduction conditions for the NiO in the anode, to obtain Ni(0), the active phase. Several reduction methods have been employed over time, both in-situ and ex-situ [2]; in our case, the chosen route was the employment of a diluted hydrogen mixture at high temperature. To make sure the anode was fully reduced, it was chosen to raise the temperature of the chamber while fluxing a 30% diluted hydrogen gas mixture in argon before proceeding in raising temperature to 700°C, at which the first measurements is carried out. The symmetric cells were taken to 550°C and stationed at that temperature for three hours to achieve full reduction of the anode, expecting that this temperature would not negatively affect the cathode. XRD patterns were obtained on powders treated for one hour in $H_2$ at 500°C, yet the conditions did not allow for a full reduction. For this reason, the temperature was raised to 550°C and the stationing time was increased up to 3 hours, just before taking the cell to a higher temperature. TPRs displaying the reduction of nickel oxide in YSZ show different behaviour depending on the state of the material, on the stoichiometric ratio between the two components and whether it is found in powder state or in a low or high temperature sintered state. For an analogous material 61% NiO in YSZ calcinated at 1450°C, the TPR main reduction peak is found at 800 K [27], just below the selected temperature of 550°C.

The reduction process is mainly a problem for complete cells, in presence of the cathode, which behaves differently from the anode in a reducing atmosphere. For LSCF, TPRs were examined to determine the temperature at which a reducing atmosphere would induce a stoichiometric variation of the material. Reduction of the material occurs at about 860°C, in particular on Co and Fe sites, while on lower temperatures, at 640°C a reduction peak is observed,

and below 400°C, only excessive non-stoichiometric oxygen is removed from inside the structure [28,29]. A modification of the structure was observed after treatment of LSCF powders up to 800°C, with a 5°C/min ramping, in a 100 sccm, 30% $H_2$ atmosphere in Ar, and cooling in pure argon flow. No specific phases were identified, but a new crystalline component did arise. A second test was carried out, though, to confirm whether or not it is possible to achieve reoxidation of the powder. Here, the commercial powder was treated in $H_2$ up to 800°C, with a 5°C/min ramping (same treatment of the previous powder sample), then kept for one hour at the same temperature in a $CH_4/O_2=2$ working gas mixture, then cooled in a pure argon flow. As the diffraction patterns reported in Figure 3 show, the structure of the powder treated with the working mixture of methane and oxygen, differently from the sample treated in hydrogen alone, shows the same crystalline structure of the commercial powders, confirming the reoxidation of the material.

# 3 Results and discussion

## 3.1 Symmetric cells

The main goal of this work was observing the effects of increasing infiltration amounts on impedance spectra and, particularly, resistance of the electrodes. Symmetric cells were tested, starting from a non-infiltrated (0wt% $CeO_2$) Ni-YSZ electrode, then 3wt%, 6wt%, 9wt% and eventually a 15wt% $CeO_2$ infiltrated cell. Cells were tested in hydrogen at three different increasing temperatures, 700°C, 750°C and 800°C, and only at 800°C the cells were also tested in the working gas mixture ($CH_4/O_2=2$). This was done to prevent the electrodes degradation given by carbon deposition that may arise with oxidation of methane or re-oxidation of the anode that may proceed with the employment of an oxidating atmosphere [21,30]. The tests on symmetric cells were planned to use a ramp of 2°C/min from room temperature to 550°C with a dwelling of 3 hours, then 1.5 hours at 700°C, 1.5 hour at 750°C and finally reaching 800°C with ramps of 2°C/min and a flow set to 100 sccm with a composition of 30% hydrogen and 70% argon. At 800°C, after the EIS measurements in hydrogen, the gas was switched to 100 sccm of a gas mixture composed of 20% in pure methane, 10% oxygen, introduced by flowing air, and argon as completion gas. Both gas mixtures went through a bubbler to humidify the mixture (about 3%) before the inlet of the chamber. The Electrochemical Impedance Spectroscopy (EIS) measurements were obtained with an Autolab PGSTAT204 (Metrohm, CH) potenziostat/galvanostat with 20 mV AC amplitude in a frequency range of $10^6$ Hz to $10^{-2}$ Hz, always displayed, for decreasing frequencies from left to right. Measurements were taken in sequence at each temperature, always with the same setting, to follow all possible variations in behaviour over time of the cells. All Area Specific Resistance (ASR) values reported are associated to circular electrodes of 1.2 cm in diameter. When possible, resistance values were obtained by fitting the curves with ZView (3.5e version). The most frequently
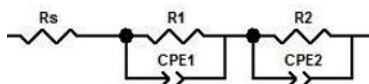
**Figure 4:** Equivalent circuit used to fit the EIS spectra. $R_S$ is associated to the resistance of the electrode, the two elements with a Resistance in parallel with a constant phase element (CPE) are associated to the semi-circles at the different frequencies.

employed associated circuit follows the scheme reported in Figure 4. It was often not possible to retrieve a resistance value from the fits because of the issues encountered with fitting specific shapes of the spectra or because of the signal instability at low frequencies, that did not allow for the semicircles to reach an ordinate value tending to 0 $\Omega$ at frequencies close to $10^{-2}$ Hz. In these cases, the resistance is determined by the difference between the lowest frequency point following the curve and the highest frequency point (with $-Z'' \geq 0$). Concerning the significant figures, always 2 are reported. Temperature increase induces a lowering in the electrolyte resistance, referred to the gap between the abscissa values of 0 $\Omega$ and that of the first point at high frequencies (with $-Z'' \geq 0$).

The cell without $CeO_2$ infiltration (0wt%), at 700°C delivers a spectrum that reaches about 300 $\Omega$ (over 160 in ASR $\Omega$ cm$^2$) a value that discourages the exploitation of the material, despite the temperature is suited for YSZ electrolytes [2,3]. At 750°C, though, the resistance is halved with an ASR of 75 $\Omega$ cm$^2$, and eventually, 40 $\Omega$ cm$^2$ at 800°C. These resistances are higher than the expected ones, in the range of a few ohms, but considering the preparation steps, the materials and the experimental conditions are the same for all measurements, they serve as a valid reference for the measurements on infiltrated cells. The spectra are reported in Figure 5, above. The employment of the chosen methane gas mixture ($CH_4/O_2=2$) drastically diminishes the resistance observed down to an ASR of 11 $\Omega$ cm$^2$. The comparison between the spectra at 800°C for the cell tested in $H_2$ and in $CH_4/O_2$ are reported in Figure 5, below.

The interpretation of the EIS spectra relies on computational models. Different works in literature link different frequency ranges to different chemical processes, so the interpretation given is not univocal. EIS spectra can change across the whole frequency range just by a change in the chemistry and the structure of the material [31]. The first semicircle on the left is that for high frequencies (HF), describing a range around $10^6$ Hz – $10^4$ Hz. This is generally described as due to charge transfer process and electrical double layer. Its value is also proportional to the triple phase boundary (TPB) density in the material [32]. The next semicircle on the right, is that for medium frequencies (MF), in a range around $10^4$ Hz – $10^1$ Hz. Sometimes it is also visible a smaller arch at the highest measured Z' values, for the low frequencies (LF), in the range $10^1$ Hz – $10^{-2}$ Hz. These two semi-circles are generally associated with mass transfer processes, the one at MF depends on the micro-structure of the material and is due to gas diffusion through the electrode and the current collector, while the LF arch is associated to the diffusion of gases on top of the electrodes [31,33].

The behaviour of the cell 3wt% $CeO_2$ infiltrated was stable in hydrogen at all temperatures, both at 700°C, 750°C and
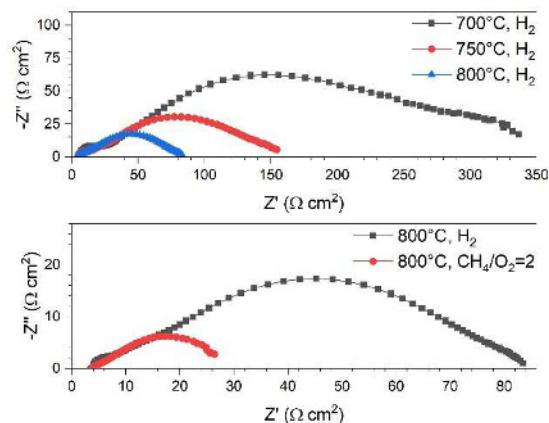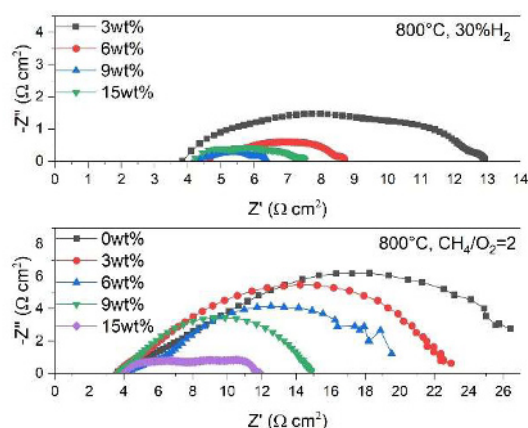


**Figure 5:** Above: EIS spectra for the 0wt% infiltrated symmetric cell at the different temperatures in $H_2$, 700°C (black), 750°C (red) and 800°C (blue). Below: EIS spectra for the same cell obtained at 800°C in $H_2$ (black) first, and in a $CH_4/O_2=2$ gas mixture (red) later.
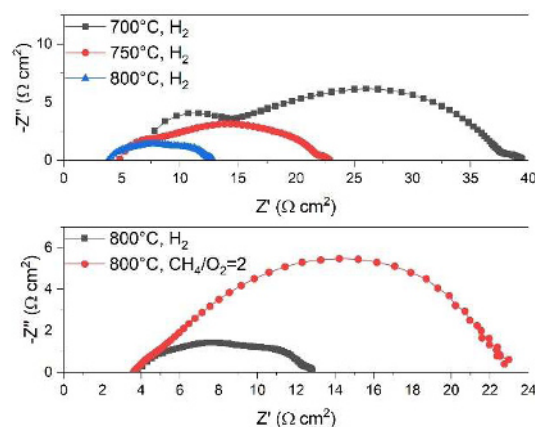


**Figure 6:** Above: EIS spectra for the 3wt% infiltrated symmetric cell at the different temperatures in $H_2$, 700°C (black), 750°C (red) and 800°C (blue). Below: EIS spectra for the same cell obtained at 800°C in $H_2$ (black) first, and in a $CH_4/O_2=2$ gas mixture (red) later. These spectra are representative of all those for infiltrated cells, all having similar behaviour qualitatively and being different only quantitatively.

800°C, not increasing their resistance over time. The Area Specific Resistance (ASR) reduction is consistent between the different temperatures: 16 $\Omega$ cm$^2$ at 700°C, 9.0 $\Omega$ cm$^2$ at 750°C and 4.8 $\Omega$ cm$^2$ at 800°C. The values reported are referred to Figure 6, above. When employing the methane gas mixture, the ASR is doubled, with a value of 9.6 $\Omega$ cm$^2$. The comparison between the spectra at 800°C for the cell (3wt%) tested in $H_2$ and in $CH_4/O_2$ are reported in Figure 6, below. In addition to the resistance, also the ordinate values of the spectra consistently increase, from 1.3 $\Omega$ to 4.8 $\Omega$, denoting a larger capacitance of the electrodes. The curves at high frequencies, though, are not relevantly different in shape, but they both appear as almost overlapped by the arches at medium frequencies, the ones displaying the largest increase in real and complex impedance values. The same trend is repeated also for all the symmetric cells whose anodes were infiltrated with larger percentages of $CeO_2$, meaning that working in

**Figure 7:** Above: comparison of the EIS spectra for the 3wt%, 6wt%, 9wt% and 15wt% infiltrated symmetric cell at 800°C in H$_2$. Below: comparison of the EIS spectra for the 0wt%, 3wt%, 6wt%, 9wt% and 15wt% infiltrated symmetric cell at 800°C in in the CH$_4$/O$_2$=2 gas mixture.

methane, for these cells, make the resistance double and the capacitance to grow larger as well. This behaviour is the exact opposite of that observed for the non-infiltrated cell in Figure 5. The reasons for this effect are unclear, but undeniably, the CeO$_2$ infiltration has an effect over this. Several hypotheses can be drawn on the matter, but the most convincing one is that CeO$_2$ strongly influences the oxidation process, taking methane to full oxidation and leaving the electrodes free from carbon; in doing so, the impedance spectra show the resistance of the electrode itself, which is expected to be higher at low frequencies because partial reforming and full oxidation of methane are more complex processes than hydrogen oxidation and because of a more size hindered transport of the gases inside the electrodes, while the cell without infiltration is not as-efficient in oxidizing methane, comporting a thin carbon layer to grow on top of the anodic material [34], which is thin enough to boost conduction. In fact, all HF and MF points in the EIS plots are found at smaller values and all high frequencies are denser for the non-infiltrated cell, while this does not happen for the infiltrated ones, where the HF semi-circles are almost superimposed (in position and density).

The cells with increased infiltration amounts, in EIS spectra measured at the three different temperatures in hydrogen, all follow the same trend observed for those with a 3wt% infiltrated CeO$_2$ infiltration, with a great reduction of both the visible semi-circle, especially the HF one. For this reason, they are not reported. All cells with

**Table 1:** ASR values obtained for the cells with increasing infiltrations, both in H$_2$ and in CH$_4$/O$_2$=2.

| CeO$_2$ infiltration | ASR in H$_2$ ($\Omega$ cm$^2$) | ASR in CH$_4$/O$_2$=2 ($\Omega$ cm$^2$) |
|---|---|---|
| 0wt% | 40 | 11 |
| 3wt% | 4.5 | 9.7 |
| 6wt% | 2.1 | 7.7 |
| 9wt% | 1.1 | 5.6 |
| 15wt% | 1.7 | 3.9 |

different infiltration amounts tested in hydrogen at 800°C are reported and compared in Figure 7, above. The cell without infiltration, with an ASR of 40 $\Omega$ cm$^2$, had a resistance that was too high compared to the other ones, so it is not reported in the graph. In Figure 7, below, the same cells, plus the non-infiltrated one, are compared for measurements carried out at 800°C employing the CH$_4$/O$_2$ gas mixture. The signal for the cells in the new environment inside the chamber takes a while before it become stable, still, some of the cells went through a quick degradation of the electrodes. To balance these boundaries, all measurements reported are acquired after about 20 minutes after the introduction of the methane gas mixture.

The ASR values observed for the different cells at 800°C, both in hydrogen and in methane, are reported in Table 1. For the cells tested in hydrogen, the resistance is constantly lowered until the 9wt% infiltrated cell, suggesting that the infiltration process helped the material to work more efficiently. Yet the 15wt% infiltrated displays a higher resistance than the 9wt% one in hydrogen. A difference that is not observed in methane, where the 15wt% one has the lowest resistance observed. This cell, it is assumed, received too much infiltration for the porosity that can be achieved with this preparation route, and the CeO$_2$ nanoparticles managed to reduce the TPB density in the anode, driving the efficiency lower. Indeed, both the HF and the MF semi-circles grow, meaning that both the charge transfer and the gas permeability in the material are negatively affected. In methane, on the other hand, the advantages of having CeO$_2$ to help methane oxidation is much more important than the reduced TPB density, as the consistent reduction of the spectrum size in CH$_4$/O$_2$ suggests. After the infiltration process in some of the 15wt% infiltrated cells, it was possible to see a faint white halo above the anode, probably due to a portion of CeO$_2$ that did not menage to enter inside the porosities and remained on top of the anode. If this is the case, infiltrations should only be used for highly porous materials or for lower amounts of CeO$_2$, otherwise, different preparation processes are recommended.

The EIS spectra in Figure 7, show that the infiltration process was successful in decreasing the resistance of the electrodes in a methane/oxygen mixture, which translates in a better performance of the material due to an increased efficiency of the physical and chemical processes involved during the employment of a SOFC with these conditions. Also, when comparing the 0wt% infiltrated cell to the others, despite the different behaviour in methane/oxygen previously discussed, its resistance turns out to be higher than those for infiltrated cells.

Despite the promising results of these tests, the ASR could still be reduced and since the MF semi-circles appear to be large enough to hide the HF and LF ones, the cells could be improved with a better control over porosity to allow a better permeation of the gas through the material.
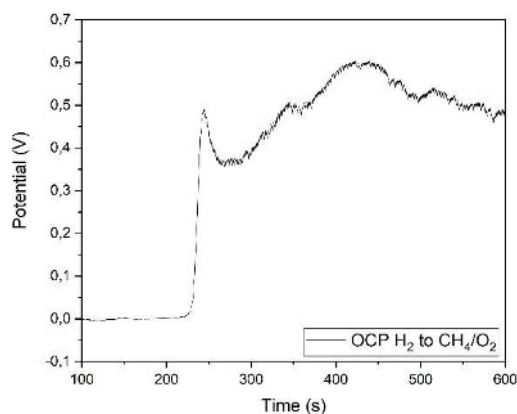
## 3.2 Complete cells

Some tests were carried out on complete cells to test their performance. Successful tests include three cells with

anodes infiltrated with 0wt%, 6wt% and 9wt% $CeO_2$. These tests were carried out with the intent to make a comparison in stability and efficiency between the different cells. As for symmetric cells, despite the working conditions and preparation process were kept the same for every cell (except for the infiltration amount), the reproducibility of the process is limited, and different parameters may change. However, the results are representative of the cells behaviour and may give several insights. The tests on complete cells followed the following steps. The cell with an unreduced anode is brought directly from room temperature to 800°C with a ramp of 2°C/min with a variable dwelling of at least 2 hours. For these cells, the degradation was very quick and, despite other data were retrieved for lower temperatures, cannot be considered reliable to a critical loss in OCP after treatment at 800°C, indicating a substantial modification of the cells that can't be described a priori, despite different processes may occur [35]. Another important effect to consider is that the LSCF-based cathode had been in contact with a reducing atmosphere for several hours. Even though the cathode, as previously explained, should quickly recover from any minor reduction, the measurements required several minutes before they could be carried out. Meanwhile, the OCP variation was a good indicator of the materials condition. Up to 800°C, the flow was set to 100 sccm with a composition of 30% hydrogen and 70% argon. At 800°C, after the EIS measurements in hydrogen, the gas was switched to 100 sccm of the same methane/oxygen gas mixture previously used for symmetric cell tests. The Electrochemical Impedance Spectroscopy (EIS) measurements, as in the previous case, were obtained in a frequency range of $10^6$ Hz to $10^{-2}$ Hz with 20 mV AC amplitude. After testing the cells in $H_2$ at 800°C, the OCP was measured, and the methane/oxygen gas mixture was introduced to keep track of its growth and the signal stability. After that, an alternation on EIS and Linear Sweep Voltammetry (LSV) measurements occurred until deactivation, after which only EIS measurements were made.

The complete cell without infiltration (0wt%) displayed the same behaviour observed for the symmetric cell counterpart, with a consistent reduction in resistance in switching from hydrogen to the methane/oxygen mixture. A comparison of the behaviour in the two atmospheres is reported in Figure 8, above. The cell at 800°C in hydrogen displayed an ASR of 30 $\Omega$ $cm^2$, while it was of 8.7 $\Omega$ $cm^2$ in $CH_4/O_2$. In the methane mixture, the cell appeared very stable, displaying a maximum observed ASR of 10 $\Omega$ $cm^2$ after 2 hours in this gas mixture, however, the performance dropped down in the same time range. In Figure 9, it is reported the OCP growth observed for this cell, with the $CH_4/O_2$ mixture being employed within the first minute. After a sharp growth, the signal proved itself unstable, with wide oscillations for some minutes, eventually stabilizing within a range of about 20 mV around 500 mV. After about 25 minutes, an OCP of 478 mV was observed, with a power of 3.7 mW $cm^{-2}$. After about 40 minutes the OCV peaked at 614 mV delivering a power of 6.7 mW $cm^{-2}$, then went back to the previous values, after about 55 minutes, with 473 mV OCP and 3.6 mW $cm^{-2}$ in power, and
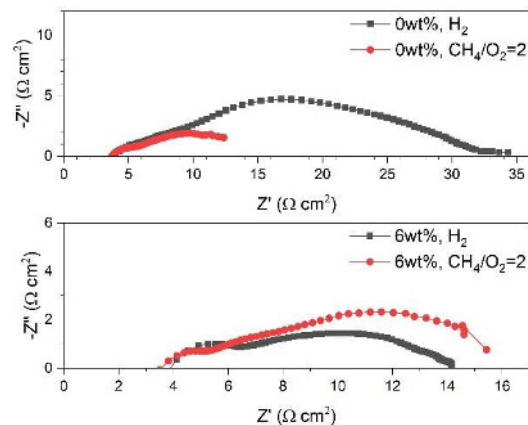


**Figure 8:** Above: comparison of the EIS spectra for the 0wt% infiltrated complete cell tested in $H_2$ and $CH_4/O_2$=2 at 800°C. Below: comparison of the EIS spectra for the 6wt% infiltrated complete cell tested in $H_2$ and $CH_4/O_2$=2 at 800°C. The 9wt% infiltrated complete cell, in the same conditions display the same behaviour shown by the 6wt%, except for the quantitative values.
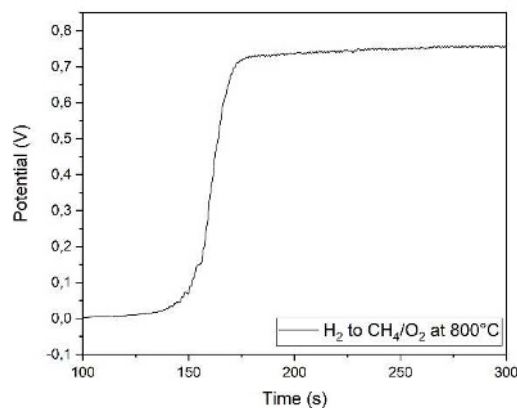


**Figure 9:** Rising and stabilization of the 0wt% infiltrated complete cell OCP after introducing the $CH_4/O_2$=2 gas mixture into the chamber.

eventually decreased to 398 mV and 2.4 mW $cm^{-2}$ after about 2 hours.

The complete cell with a 6wt% $CeO_2$ infiltration at the anode was the most unstable of the complete ones. The ASR at 800°C in $H_2$ was 10 $\Omega$ $cm^2$, higher than the value obtained for the non-infiltrated cell, then it rose to 12 $\Omega$ $cm^2$ after about 30 minutes in $CH_4/O_2$, showing again a behaviour with the gas switch that is the opposite of that observed for the 0wt% complete cell. These results are shown in Figure 8, below, and can be compared to the results for the 0wt% cell in the graph above. After a couple of hours, the ASR increased up to 20 $\Omega$ $cm^2$, almost doubling the initial resistance. The OCP was very unstable, with oscillations up to 30 mV after about 10 minutes in $CH_4/O_2$. After 30 minutes of methane gas mixture flowing in the chamber, an LSV measurement showed an OCP of 610 mV and a power of 5.6 mW $cm^{-2}$. The OCP and the power quickly decreased and after about 70 minutes it reached 435 mV in OCP and 3.0 mW $cm^{-2}$ in power. Eventually, after a couple of hours the OCP dropped below 200 mV. A test was carried out to attempt a re-activation

**Figure 10:** Rising and stabilization of the 9wt% infiltrated complete cell OCP after introducing the $CH_4/O_2=2$ gas mixture into the chamber.



**Figure 11:** LSV and power obtained after about 20-25 minutes from the employment of the $CH_4/O_2=2$ gas mixture for the 0wt%, 6wt% and 9wt% complete cells. A correlation between increasing OCP and power with the increasing amount of infiltration can be observed.

of the material in hydrogen, but after the $CH_4/O_2$ mixture was re-introduced, it did not manage to make the OCP increase again, as is remained below the 100 mV.

The complete cell with an anode infiltration of 9wt% $CeO_2$ managed to deliver the highest power of the three cells. At 800°C in $H_2$ the cell displayed an ASR of 2.9 $\Omega$ cm$^2$ that rose to 4.3 $\Omega$ cm$^2$ after the $CH_4/O_2$ mixture was employed. These values are low compared to the previous ones for complete cells, yet the EIS measurement in methane had an unstable signal. The instrument was unable to retrieve meaningful data around frequencies of 5 Hz, with the beginning of the LF range. So, the last point following the trend was chosen as limit for determining the ASR. Despite the instability of EIS spectra at LF, the OCP measured with the transition between the two gas mixtures was the most stable with oscillations below 10 mV, as shown in Figure 10. After 20 minutes stabilization, LSV measurements determined an OCP of 766 mV and a power of 13.3 mW cm$^{-2}$. The cell was stable enough to avoid a constant drop in performance, despite temporary losses, and reaching the highest values of OCP and power of 776 mV and 14 mW cm$^{-2}$. Eventually, after a couple of hours, the cell abruptly broke, delivering meaningless values.

In comparing the results for the different complete cells, it is chosen to look at the results obtained after about 20-25 minutes after switching to the methane/oxygen gas mixture, neglecting the best performances obtained, being transient phenomena, and considering the quick degradation that the cells face, especially the 6wt% one. With these considerations, in Figure 11, it is seen the correlation between an increased performance and an increasing amount of infiltrated $CeO_2$ into Ni-YSZ cermet anodes. For more consistent results, further tests with other infiltration percentages should be carried out.

An issue that occurred for all cells used in a methane/oxygen mixture at 800°C was a quick degradation of the cells. The problem is supposed being due to surface segregation of anodic Ni on top of the gold paste employed. This hypothesis is confirmed by X-ray Photoelectron Spectroscopy (XPS) measurements, where on top of the cell, where nothing but gold should be seen, almost no gold was found and nickel is present, while above the scratched surface, the spectra revealed the
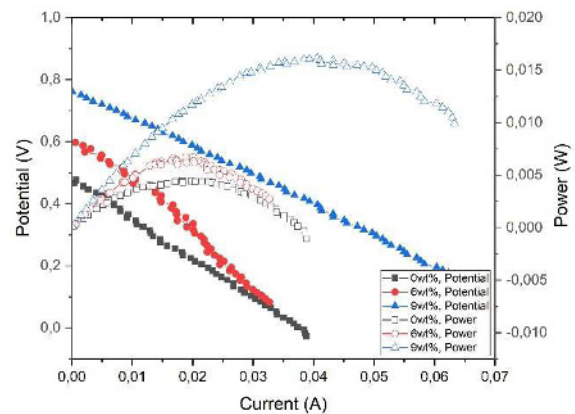
absence of nickel and presence of gold, with the patterns being the same as those obtained on the gold paste that was not deposited in contact with the anode. However, the results of these tests are not reported since this work does not discuss on the current collector properties.

## Conclusions

The correlation between performance and increasing $CeO_2$ infiltration amounts in Ni-YSZ anodes in SC-SOFCs was tested. In symmetric cells, low percentage infiltration amounts drastically decreased the resistance of the electrodes in $H_2$, with best results for the 9wt% cell. Increasing infiltration induced a continuous improvement in $CH_4/O_2=2$, with best results for the 15wt% cell, with a reduction of EIS spectra semi-circles both at HF and MF. Complete cells confirmed the observations on symmetric cells, with increased performance for higher infiltrations, both in OCP and power, despite transient instabilities in performance. EIS tests were not as clarifying, even though they were not against the trend observed for symmetric cells. However, measurements on complete cells were not comprehensive of the whole infiltration range tested for symmetric cells and results should be confirmed.

## Acknowledgements

## References

[1] A. Hagen, A.C. Wulff, P. Zielke, X. Sun, B. Talic, I. Ritucci, H.L. Frandsen, S.H. Jensen, W.R. Kiebach, P. V. Hendriksen, Int. J. Hydrogen Energy **45** (2020) 29201–29211.

[2] M. Kuhn, T.W. Napporn, Energies **3** (2010) 57–134.

[3] M. Yano, A. Tomita, M. Sano, T. Hibino, Solid State Ionics **177** (2007) 3351–3359.

[4] I. Riess, J. Power Sources 175 (2008) 325–337.

[5] Y. Hao, D.G. Goodwin, J. Power Sources **183** (2008) 157–163.

[6] M. Kamvar, M. Ghassemi, R. Steinberger-Wilckens, Int. J. Hydrogen Energy **45** (2020) 7077–7087.

[7] Z. Shao, S.M. Haile, J. Ahn, P.D. Ronney, Z. Zhan, S.A. Barnett, Nature **435** (2005) 795–798.

[8] B. Morel, Ŕ. Roberge, S. Savoie, T.W. Napporn, M. Meunier, Electrochem. Solid-State Lett. **10** (2007) 2006–2008.

[9] L.N. Van Rij, J. Le, R.C. Van Landschoot, J. Schoonman, J. Mater. Sci. **36** (2001) 1069–1076.

[10] M. Yano, M. Nagao, K. Okamoto, A. Tomita, Y. Uchiyama, N. Uchiyama, T. Hibino, Electrochem. Solid-State Lett. **11** (2008) 29–33.

[11] Y. Lu, Y. Liu, S. Shen, J. Catal. **177** (1998) 386–388.

[12] C. Zhang, Y. Lin, R. Ran, Z. Shao, Int. J. Hydrogen Energy **35** (2010) 8171–8176.

[13] Z. Jiao, N. Shikazono, N. Kasagi, J. Electrochem. Soc. **159** (2012) B285–B291.

[14] B. Morel, R. Roberge, S. Savoie, T.W. Napporn, M. Meunier, J. Power Sources **186** (2009) 89–95.

[15] T. Hibino, A. Hashimoto, M. Yano, M. Suzuki, S. Yoshida, M. Sano, J. Electrochem. Soc. **149** (2002) A133.

[16] M.D. Cabezas, D.G. Lamas, M.G. Bellino, R.O. Fuentes, N.E. Walsöe De Reca, S.A. Larrondo, Electrochem. Solid-State Lett. **12** (2009) 35–38.

[17] C. Zhang, L. Sun, R. Ran, Z. Shao, Electrochem. Commun. **11** (2009) 1563–1566.

[18] A. Trovarelli, Catal. Rev. **38** (2006) 439–520.

[19] H. Takahashi, T. Takeguchi, N. Yamamoto, W. Ueda, Solid State Ionics **185** (2011) 52–57.

[20] G. Yang, C. Su, W. Wang, R. Ran, M.O. Tadé, Z. Shao, J. Power Sources **264** (2014) 220–228.

[21] Z. Wang, Z. Lü, B. Wei, K. Chen, X. Huang, W. Pan, W. Su, Electrochim. Acta **56** (2011) 6688–6695.

[22] D. Rembelski, J.P. Viricelle, L. Combemale, M. Rieu, Fuel Cells **12** (2012) 256–264.

[23] A. Atkinson, A. Selçuk, Acta Mater. **47** (1999) 867–874.

[24] S.Y. Park, J.H. Ahn, C.W. Jeong, C.W. Na, R.H. Song, J.H. Lee, Int. J. Hydrogen Energy **39** (2014) 12894–12903.

[25] A. Chen, J.R. Smith, K.L. Duncan, R.T. DeHoff, K.S. Jones, E.D. Wachsman, J. Electrochem. Soc. **157** (2010) B1624.

[26] S. Elangovan, J.J. Hartvigsen, L.J. Frost, Int. J. Appl. Ceram. Technol. **4** (2007) 109–118.

[27] H. Mori, C.J. Wen, J. Otomo, K. Eguchi, H. Takahashi, Appl. Catal. A Gen. **245** (2003) 79–85.

[28] A.P. Jamale, C.H. Bhosale, L.D. Jadhav, J. Alloys Compd. **623** (2015) 136–139.

[29] L.F. Liotta, F. Puleo, V. LaParola, S.G. Leonardi, N. Donato, D. Aloisio, G. Neri, Electroanalysis **27** (2015) 684–692.

[30] A. Faes, A. Hessler-Wyser, A. Zryd, J. Van Herle, Membranes (Basel). **2** (2012) 585–664.

[31] S. Gewies, W.G. Bessler, J. Electrochem. Soc. **155** (2008) B937.

[32] B. Song, E. Ruiz-Trejo, A. Bertei, N.P. Brandon, J. Power Sources **374** (2018) 61–68.

[33] A. Bertei, E. Ruiz-Trejo, F. Tariq, V. Yufit, A. Atkinson, N.P. Brandon, Int. J. Hydrogen Energy **41** (2016) 22381–22393.

[34] A. Lanzini, P. Leone, C. Guerra, F. Smeacetto, N.P. Brandon, M. Santarelli, Chem. Eng. J. **220** (2013) 254–263.

[35] X. Jacques-Bédard, T.W. Napporn, R. Roberge, M. Meunier, J. Power Sources **153** (2006) 108–113.